Matter

Self-sensitizable neuromorphic device based on adaptive hydrogen gradient

Tao Zhang[1,15], Mingjie Hu[1,15], Md Zesun Ahmed Mia[2], Hao Zhang[3], Wei Mao[4,5], Katsuyuki Fukutani[4], Hiroyuki Matsuzaki[5,6], Lingzhi Wen[7], Cong Wang[8], Hongbo Zhao[1], Xuegang Chen[9], Yakun Yuan[10], Fanqi Meng[11], Ke Yang[12], Lili Zhang[12] Juan Wang[12], Aiguo Li[12], Weiwei Zhao[13], Shiming Lei[14], Jikun Chen[3,*], Pu Yu[7], Abhronil Sengupta[2], and Hai-Tian Zhang[1,16,*]

[1]*School of Materials Science and Engineering, Beihang University, Beijing 100191, China*
[2]*Department of Electrical Engineering, The Pennsylvania State University, University Park, PA 16802, USA*
[3]*School of Materials Science and Engineering, University of Science and Technology Beijing, Beijing 100083, China*
[4]*Institute of Industrial Science, The University of Tokyo, Meguro-ku, Tokyo 153-8505, Japan*
[5]*School of Engineering, The University of Tokyo, Bunkyo-ku, Tokyo 113-0032, Japan*
[6]*Micro Analysis Laboratory, Tandem Accelerator (MALT), The University Museum, The University of Tokyo, Bunkyo-ku, Tokyo 113-0032, Japan*
[7]*State Key Laboratory of Low Dimensional Quantum Physics and Department of Physics, Tsinghua University, Beijing 100084, China*
[8]*School of Materials Science and Engineering, Anhui University, Hefei 230601, China*
[9]*Center of Free Electron Laser & High Magnetic Field, Institutes of Physical Science and Information Technology, Anhui University, Hefei 230601, China*
[10]*Zhangjiang Institute for Advanced Study, Shanghai Jiao Tong University, Shanghai 200240, China*
[11]*School of Materials Science and Engineering, Peking University, Beijing 100871, China*
[12]*Shanghai Synchrotron Radiation Facility, Shanghai Advanced Research Institute, Chinese Academy of Sciences, Shanghai 201204, China*
[13]*Sauvage Laboratory for Smart Materials, School of Materials Science and Engineering, Harbin Institute of Technology, Shenzhen 518055, China*
[14]*Department of Physics, The Hong Kong University of Science and Technology, Kowloon, Hong Kong SAR 999077, China*
[15]*These authors contributed equally to this work*
[16]*Lead contact*

[*]*Correspondence: jikunchen@ustb.edu.cn (J.C.); htzhang@buaa.edu.cn (H.-T.Z.)*

Existing neuromorphic computing systems have always faced a longstanding challenge: when confronted with drastic environmental variations and unknown circumstances beyond the pre-set boundaries, they would inevitably suffer from substantial information loss and catastrophic model failure. In contrast, the human brain employs a neural adaptive self-sensitization mechanism to actively grasp critical information in changing environments, addressing these problems effortlessly. However, previous brain-inspired hardware lacked the capacities to seek out essential information across diverse inputs, often confined to passive responses within unalterable boundaries. Here, we report the adaptive self-sensitization in hydrogen-doped perovskite neurons based on versatile hydrogen gradient distributions, which transcends the fixed response range of conventional artificial neurons to autonomously capture previously unrecognized information. Therefore, the networks with self-sensitizable neurons can adaptively handle intricate tasks under turbulent and unknown environments by reshaping the information reception range and feature salience. It can address the issue of information loss and achieve seamlessly transition, processing ~250% more structural information than normal networks in building and vehicle detection. Furthermore, the self-sensitizable convolutional network can surpass model boundaries to tackle the persistent challenge of data drift accompanying varying inputs, improving accuracy by ~110% compared to traditional networks in vehicle classification. The self-sensitizable neuron enables the networks to autonomously cope with unforeseen environments, opening new avenues for self-guided cognitive systems.

Keywords: neuromorphic device, self-sensitization, edge detection, spiking neural network

INTRODUCTION

Brain-inspired or neuromorphic computing is a new technology paradigm that aims to perform highly efficient computations based on neural networks[1–6]. In a neural network, neurons, the computing units, are interconnected by numerous synapses and have the potential to overcome the von Neumann Bottleneck where the computing unit and the memory are separated[7–13]. Nowadays, it is widely acknowledged that the brain's operation involves more than just simple nonlinear functions mapping between input and output, such as those used in deep neural networks (DNNs), no matter how complex or deep they may be[14–17]. Over millions of years of evolution, the biological brains have developed rich functionalities such as stochasticity, synchronizability and self-sensitization[18–21]. These characteristics enable them to process information more flexibly and make wiser decisions when faced with dynamic and complex environments, thereby coping better with various survival challenges[22–24]. For instance, the biological brains exhibit remarkable adaptability in processing visual input signals under varying lighting conditions. When transitioning into darkness, they can dynamically adapt to the environmental change and enhance their ability to effectively recognize objects[25]. They also display adaptive sensitization to detailed auditory signals in noisy environments, enabling them to discern specific sounds with heightened accuracy and clarity[26,27]. A crucial mechanism underlying these significant capabilities in biological brains is the neuron self-sensitization, which facilitates versatile handling of critical details and varying features in diverse environments, enabling them to possess high levels of cognition and decision-making abilities[28,29].

In contrast, existing neuromorphic computing in AI has consistently lacked these excellent capabilities similar to biological brain, resulting in inevitable information loss and catastrophic model failure when facing drastic environmental changes exceeding predefined boundaries. For instance, abrupt weather changes could lead to critical traffic information loss, resulting in severe accidents in autonomous driving systems. Disaster rescue AI machines may fail to work in unforeseen scenarios beyond pre-set produces. Therefore, faithfully emulating the biological self-sensitization will be a critical approach to address these significant challenges in existing artificial intelligence. However, previous brain-inspired devices lacked the capacities to autonomously seek out essential information among environmental changes, often confined to passive responses to external signals. These artificial neurons were also frequently constrained by a limited signal reception range, exhibiting limited adaptability when transitioning into various surroundings.[30–35]

In this work, we report the self-sensitization mechanism based on perovskite nickelate artificial neurons, which can surpass the constrained signal reception range of conventional artificial neurons, autonomously perceiving environmental changes and capturing previously unrecognizable information through adaptive neuron activation function shift. This self-adaptive functionality stems from the complexity and multiplicity of hydrogen gradient distributions under electric pulse signals, enabling versatile responsiveness to different inputs, as shown in **Figure 1(A)**. The networks with the self-sensitizable neurons can handle challenging edge detection and object classification tasks under drastic and unforeseen variations of lighting conditions, where the computing resources were adaptively reorganized in response to the dynamic input data. In edge detection of buildings and vehicles, it exhibited autonomous recognition of different inputs, transcending the limitation of information loss faced by normal networks in complex environmental changes. The self-sensitizable network can capture and process ~250% more information content, performing well in bright environments and adaptively reshaping its information reception range to seamlessly adapt to the dark environments. Furthermore, the self-sensitizable convolutional neural network can tackle the challenge of data drift resulting from varying inputs that exceed predetermined training ranges. In vehicle classification, it achieved ~110% improvement in recognition and decision-making capabilities compared to normal networks through autonomously remolding the feature salience in ever-changing circumstances. The contrasting effects in changing environments can be directly observed in **Figure 1(B).** We demonstrate that the self-sensitizable neurons endow the networks with cognitive capacities to process ever-changing information flexibly and efficiently, unveiling the future potential of incorporating bio-inspired traits in artificial intelligence systems.

RESULTS AND DISCUSSION

Experimental self-sensitization of stochastic neurons.

Perovskite nickelates are a category of Mott quantum materials with strong electron-electron correlations and undergoes an electronic metal-to-insulator phase transition at room temperature upon hydrogen doping[36,37]. For instance, in $NdNiO_3$ (NNO) with catalytic electrodes (Pd), hydrogen can be infused into the NNO lattice through annealing in a hydrogen gas atmosphere. Hydrogen atoms then contribute electrons to Ni d band, leading to a modification in electron filling state and a change in resistivity spanning several orders of magnitude[38]. Furthermore, the hydrogen ion distribution can be adaptively adjusted under the influence of electric fields, leading to pronounced alterations of electrical properties[39,40]. Therefore, the NNO neuron exhibits potential for achieving adaptive self-sensitization that can perceive and adapt to variations in environmental signals. For more detailed information about the materials and devices, see **Figures S1-S5**.

The experimental measured self-sensitization properties based on the perovskite device are summarized in **Figure 2**. The stochastic neuron can generate spikes with a sudden resistance change under electric pulses, as shown in **Figure 2(A)**. The spiking probability of the perovskite neuron follows a sigmoid distribution which is commonly seen in biological nervous systems, as shown in **Figure 2(B)** and **Figure S6**. To demonstrate the functionality of self-sensitization, we selected a 0.19 V/μm pulse field to stimulate the artificial neuron which initially showed a very low spiking probability. Subsequently, when several pulses were accumulated without applying any reverse reset pulses, we observed that the device exhibited adaptation to these weak signals, transitioning from a state of low spiking probability to a new state of higher spiking probability, as shown in **Figure 2(C)**. We define neuron state before it adapts to weak pulses as the initial state, and the state after self-sensitization as the self-sensitized state. This phenomenon of self-sensitization indicates that neurons can adaptively adjust their activation functions to enhance sensitivity to weak signals.

Furthermore, we observed that the perovskite neuron can achieve different sensitized states by accumulating diverse signals, as shown in **Figure 2(D)**. It suggests that the neuron can adaptively enhance its spiking ability to weak signals, expanding the range of signal reception, as shown in **Figure S7**. It is worth noting that the device does not respond to all weak signals from the external environment. When we applied very weak signals to stimulate the neuron, it did not exhibit adaptive activation function shift even after more than thirty repetitions, which means the neurons can selectively filter out background noise with low intensity, as shown in the bottom right figure of **Figure 2(D)**. Then we measured the spiking probability distribution functions of varying sensitized states and observed different probability distributions accordingly, as shown in **Figure 2(E)**. Furthermore, the neuron exhibits varying degrees of adaptive activation function shift in different sensitized states which can be represented by the spiking threshold variations, as shown in **Figure 2(F)**. The results can be repeated on the same device and reproduced from different devices, confirming the consistent self-sensitization characteristics, as shown in **Figures S8-S12**. More detailed statistical and quantitative analyses of the device functionalities were conducted to demonstrate good stability and uniformity, as shown in **Figures S13-S16.** Besides, the H-NNO device still remains the function of generating spiking behaviors after 10^6 cycles of endurance measurement, as shown in **Figure S17**. Our experimentally measured self-sensitization suggests that the perovskite neuron can adaptively adjust its neuron states to surpass the normally constrained range of signal reception, capturing previously unrecognized signals.

Microscopic origins of the self-sensitization.

To understand the microscopic mechanism of the self-sensitization in perovskite neurons, we conducted various experiments to explore the distinctions between different neuron states. The nuclear reaction analysis (NRA) experiment was performed on vertical nickelate devices[41]. NRA offers a nearly exclusive way to date to quantify the absolute amount of hydrogen directly within a solid, which provides direct evidence of hydrogen doping profile[41], and a schematic is shown in **Figure 3(A)**. The results revealed the spontaneous diffusion of hydrogen along the material's thickness direction, leading to a distinct gradient distribution, as shown in **Figure 3(B)**. The pronounced minima and maxima of hydrogen concentration near the film surface are due to the near surface instrumental functions and the adsorption of native hydrogen (e.g., H_2O)[41–43].

Next, the micro-X-ray absorption spectroscopy (micro-XAS) experiments were performed on the in-plane nickelate devices to explore the changes in the electronic structure after hydrogen doping, as shown in **Figure 3(C)** and **Figure S18**. We collected Ni K-edge energy spectra of a H-doped NNO sample at different positions near the Pd electrode and a gradual decrease of the Ni K-edge peak energy towards the Pd electrode was observed, which is attributed to the slight decrease of Ni valence state caused by the injection of additional electrons through hydrogen doping[38,44], shown in **Figure 3(D)**. The Ni K-edge peak positions for the non-spiking and spiking neuron states, as well as the pristine sample (no H-doping) are shown in **Figure 3(E)**. No peak position change was observed near the Pd electrode for the pristine sample. However, a distinct difference in the shift of the K-edge peak energy was observed between the spiking state and the non-spiking state. A larger energy peak decrease in the non-spiking state indicates a higher concentration of hydrogen ions in the device channel, leading to a higher resistance state, consistent with the electrical measurements.

Subsequently, conducting atomic force microscopy (cAFM) experiments were performed to further validate the self-sensitization mechanism stemming from the different distributions of hydrogen ions[45]. We characterized the variations in channel resistance at different positions by measuring current maps within a microregion of 1.5 μm^2 in different neuron states, providing insights into the different distributions of hydrogen ions, as shown in **Figures 3(F)-(I)**. After hydrogen doping, a gradient in conductivity of the NNO device can be observed directly near the Pd electrode (top of the figure), as shown in **Figure 3(F)**. The evident change in current gradient between the pristine sample and the H-doped sample within a range of several hundred nanometers in the device channel is illustrated in **Figure 3(G)** and **Figures S19-S20**, confirming the significant impact of hydrogen doping in conductivity. **Figure 3(H)** shows the difference in current drop near the Pd electrode for the non-spiking and spiking neuron states, suggesting varying hydrogen content corresponding to different neuron states, in alignment with the findings from the micro-XAS experiments. Furthermore, through cAFM experiments conducted on the initial and self-sensitized states, we observed a clear difference in the slope of the normalized current, indicating variations in the distribution of the hydrogen gradient, as shown in **Figure 3(H)**. These findings play a pivotal role in elucidating the mechanism of self-sensitization in perovskite neurons.

Applications of self-sensitizable neurons in AI.

To test the practicality of self-sensitizable neurons, we utilized experimental data of varying activation functions that adaptively shift based on diverse signals to simulate the self-sensitizable behaviors in the circuit simulation and neural network. When encountering different weak signals, the neurons exhibited adaptive states adjustment to increase sensitivity to these signals, as shown in **Figures 4(A)-(C)** and **Figure S21**. This characteristic will enable the neural networks to autonomously perceive various inputs, adapting seamlessly to different environments. To initially illustrate the impact of self-sensitizable neurons on neural networks, we constructed a simple fully connected self-sensitizable spiking neural network (without convolutional layers) for the classification tasks with the standard Fashion MNIST dataset[46]. This dataset features simple edge information of objects, allowing for a preliminary validation of the self-sensitizable network's adaptability. The self-sensitizable networks exhibited an improvement in accuracy compared to normal networks on datasets with normal brightness, while the improvement became significantly more pronounced when dealing with datasets in dark environments, as shown in **Figures 4(D)-(E)**. Furthermore, the enhancement in accuracy became increasingly prominent with continuous variations in environmental brightness, as shown in **Figure 4(F)**. More detailed sensitivity analysis and time/energy quantification of the self-sensitizable neuron were shown in **Figures S22-S23.** The self-sensitizable networks demonstrate their potential for adaptive adjustment in response to environmental changes using standard datasets, thereby opening up the possibilities for tackling more challenging tasks, including edge detection and image classification with abundant and complex information.

To better demonstrate the adaptive capabilities of the self-sensitizable neurons in complex environments, we implemented the experimental data to develop an enhanced edge detection algorithm, which can adaptively detect edge information of objects in varying environments. The networks with self-sensitizable neurons showcase seamless adaption to complex lighting conditions, overcoming the limitations of normal networks that struggle to handle dynamic input changes, thereby avoiding the loss of crucial details during transitions. The improved vehicle edge detection performance of self-sensitizable networks in different environments compared to the normal networks can be clearly observed in **Figure 5(A)**. To demonstrate the versatile capabilities of the adaptive network and augment the diversity of input information, we employed Stable Diffusion AI models to create extensive datasets comprising various vehicle images, including sedans, pick-up trucks, SUVs, airplanes, captured under diverse lighting conditions, as shown in **Figure S24**.

The edge information of vehicles is often intricate and diverse, and the self-sensitizable neurons empower the networks to adaptively adjust neuron states to capture and extract complete edge information, as shown in **Figure 5(B)**. The diverse neuron states in the networks were obtained from the experimentally measured self-sensitization data of the perovskite neurons. The self-sensitizable networks captured more detailed information that was often missed by normal networks due to the constrained range of signal reception, improving edge continuity and the integrity of object structures. Subsequently, to further investigate the mechanism of the self-adaptive learning in networks, we extracted the intensity distribution of inputs in both bright and dark environments, as well as the spiking probability of two types of neurons in response to different environments, as shown in **Figures 5(C)** and **5(D)**. In the bright environment, the spiking probability distribution of the self-sensitizable neurons indicates that the network redistributed the computing resources to enhance the sensitivity to detailed information while maintaining responsiveness to strong signals, resulting in good edge detection performance. Notably, when transitioning into the dark environment, the self-sensitizable neurons adaptively adjusted their states based on variations of signal intensity to reshape the reception range, generating a new peak of signal reception to capture the weak information that normal neurons could not recognize. These characteristics of self-sensitizable neurons equip the networks with the capacities to autonomously handle environmental variations and smoothly transition between different lighting conditions. Additionally, while self-sensitizable neurons enhance sensitivity to weak signals, they actively reduce the spiking probability for extremely weak signals, effectively filtering out background noise and preventing its interference with edge information, as shown in **Figures 5(C)** and **5(D)**. We further conducted a comparison of the spiking activity between normal and self-sensitizable neurons in different input conditions, as shown in **Figure 5(E)**. The results demonstrated the increase in spiking activity exhibited by self-sensitizable neurons compared to normal neurons, providing further confirmation of their enhanced information capture and processing capabilities in diverse environments.

Furthermore, we conducted a comparison of connectivity in the edge detection results obtained from different networks, which is an important indicator for evaluating the interconnection of edge information at the pixel level, as shown in **Figure 5(F)**. The findings revealed that the self-sensitizable network was capable of discerning rich details when transitioning into dark environments, ensuring the continuity and integrity of detailed edge information. We also demonstrated the capability of the self-sensitizable network to delineate more complete edge structures of diverse objects in dynamic environments through comparisons of structural phase coherence and edge length, as shown in **Figures S25-S27**. These characteristics empower self-sensitizable networks with vast prospects for applications in intricate real-world environments, such as license plate recognition in various lighting conditions and animal tracking in dynamic environments, as shown in **Figure 5(G)** and **Figures S28-S29**. In order to further quantify the advantages of self-sensitizable neurons in edge detection, we developed a vehicle classification neural network that relied on edge information, with which we tested the outputs of edge detection networks with either self-sensitizable or normal neurons in dynamic environments. The edge information output from the self-sensitizable neurons exhibited good accuracy in the vehicle classification neural network, with relative improvements of 62.1% for SUV-plane, 54.4% for pickup-plane, and 74.7% for sedan-plane, as shown in **Figure 5(H)**. These results suggest that the self-sensitizable network captures more vehicle edge information and provides the classification neural network with more discriminative features, resulting in higher accuracy of vehicle classification.

We further validated the potential of self-sensitizable neurons in tackling more complex tasks under ever-changing circumstances. With the adaptive characteristics of these neurons, the self-sensitizable network can seamlessly adapt to dynamic environments and extract ~250% more information content of subjects within the surroundings in detection of intricate buildings, addressing the issue of information loss suffered by normal networks in varying lighting conditions, as shown in **Figures 6(A)** and **6(B)**. Therefore, based on these advantages of self-sensitizable neurons, we utilized experimental data to establish a spiking convolutional neural network for vehicle classification, which can extract crucial information in diverse environments and uphold a superior level of classification accuracy. When the environmental intensities undergo alteration, the self-sensitizable convolutional layers provide more distinct features compared to normal convolutional network, as shown in **Figure 6(C)** and **Figure S30**. We compared the outputs of neurons between two types of networks in different surroundings, as shown in **Figures 6(D)-(E)** and **Figure S31**. The self-sensitizable neurons can adaptively reshape the information reception range according to different environmental intensities, enabling the convolutional networks to maintain a high subject-environment distinctiveness. In contrast, the normal neurons limited by their constrained information content, struggled to adapt to the changing data distribution within dynamic surroundings, resulting in a significant decrease in subject-environment distinctiveness. Subsequently, we used Gradient-weighted Class Activation Mapping (Grad-CAM) to study the advantages of self-sensitizable networks in classification tasks, which is an important method to assess the contribution of different features to classification decisions. The self-sensitizable convolutional network can remold the feature salience based on shifting environmental intensities, resulting in accurately recalibrating recognition emphasis to focus on the crucial subject during classification. Conversely, the normal convolutional network, lacking the ability to distinguish the subject and the environment when transitioning into dark surroundings, failed to concentrate on the correct locations and could not make accurate classification, as shown in **Figures 6(F)-(G)** and **Supplemental Figure 32**. Finally, we conducted classification tests on the two types of networks using images with various proportions of bright and dark environments. The self-sensitizable network maintained a high classification accuracy of ~90% across varying environments and outperformed the normal network by ~110% in dark surroundings, as shown in **Figure 6(H)**. These results illustrate that the self-sensitizable network achieves autonomous information processing and seamless adaptation across diverse environments, surpassing the predefined model boundaries to tackle the problem of data drift resulting from varying inputs. More details can be found in **Supplemental experimental procedures.** Furthermore, to demonstrate the widespread applicability of the self-sensitizable neural network, we also performed sound recognition tasks and achieved a high level of accuracy, as shown in **Figure S33**. Additionally, the H-NNO device was fabricated by standard CMOS technology and exhibits excellent compatibility with Si and SiO_2 substrates[47]. The compatibility allows the device to integrate seamlessly with existing semiconductor processes, providing greater flexibility and functionality for electronic system design.

Conclusion

In conclusion, we have demonstrated artificial self-sensitizable neurons can surpass the inherent limitation of passive signal reception with an unalterable range in traditional neurons, enabling to autonomously seek out and process critical information across drastic environmental changes. The bio-inspired self-sensitization is accomplished by precisely modulating ordered microstructures, such as the hydrogen gradient, a strategy readily applicable to enhance performance or introduce new functionalities in other material systems and devices. Furthermore, based on these device characteristics, we have constructed improved edge detection algorithm and classification neural network capable of adapting to intricate environments, tackling the challenges of inevitable information loss and data drift faced by conventional networks under complex and varying inputs. These results showcase the potential of self-sensitizable devices in artificial intelligence architectures operating amid intricate real-world scenarios, offering new opportunities for the realization of highly intelligent systems with autonomous cognitive capabilities.

EXPERIMENTAL PROCEDURES

Resource availability

Lead contact

Further information and requests for resources should be directed to and will be fulfilled by the lead contact, Hai-Tian Zhang (htzhang@buaa.edu.cn)

Materials availability

This study did not generate new unique reagents.

Data and code availability

The data that support the findings of this study are available from the lead contact upon reasonable request.

Method

Film growth

The $NdNiO_3$ thin films were grown on $LaAlO_3$ (001) substrates using a metal organic decomposition (MOD) approach, as described in our previous report[48]. In brief, Nd $(AC)_3$ or Ni $(AC)_2$ first reacted with $C_7H_{15}COOH$ and ammonia to form $Nd(C_7H_{15}COO)_3$ and $Ni(C_7H_{15}COO)_2$, which were used as the chemical precursors for the MOD process. These chemical precursors were mixed at equal stoichiometry and dissolved in xylene at 0.1 mol/L, and spin-coated on $LaAlO_3$ (001). Afterwards, the samples were annealed under 15 MPa oxygen pressure at 450 °C for the decomposition of the metal organic precursors, and then annealed under the same pressure at 850 °C for 2 hours to crystalize the material.

Fabrication of $NdNiO_3$ devices

The device was fabricated by the standard ultraviolet photolithography technology. A thick photoresist film (AZ5214) was deposited by spin coating at 7000 rpm for 60 seconds and then baked at 110 °C for 240 seconds at the beginning. Next, UV-exposure was performed with standard ultraviolet photolithography technology (URE-2000/35L, Institute of Optoelectronics Technology, Chinese Academy of Sciences). The photoresist was developed in the developer (prepared by AZ400K and DI water, the ratio of AZ400K and DI water is 1: 5) for 50 seconds and then soaked in DI water for 10 seconds. The developed photoresist was then etched away by ion beam etching (IBE) to leave only the rectangular nickelate channel on the substrate, and the remaining parts are insulating $LaAlO_3$ substrate. Finally, the left square electrode was exposed by negative gel sleeve engraving, followed by Au electrode (50 nm) deposition through thermal evaporation. The right electrode is exposed by the same method and then the atomically flat Pd electrodes (50 nm) were deposited by electron beam evaporation. The H-NNO device channel length is 20 μm. The $NdNiO_3$ devices studied in this work were annealed in a forming gas atmosphere ($4\%H_2/96\%N_2$) at 120 °C for 5 minutes. The hydrogen was doped at the catalytic Pd electrode through the so-called hydrogen spillover process.

Electrical measurements

Electrical measurements of the perovskite devices were performed using an XMT-600 micromanipulator probe station at room temperature. The probe station was placed on a DVT-2000 vibration isolation table to minimize noise caused by vibrations. The Tektronix AFG31000 series arbitrary function generator and the Keithley 2636B were used to perform neuron stimulation measurements, and ultra-low noise triaxial cables were used to minimize noise interference during the measurement. The resistance value of the device was obtained by fitting the voltage-current curve within the linear range of -0.1 V to 0.1 V. The measurement process was controlled by LabVIEW programs. All applied electric fields were referenced to the Au electrode.

Characterization of the as-grown nickelate film

The crystal structure of as-grown nickelate films were measured by X-ray diffraction (Rigaku D/max2500H, Japan). The cross-section morphologies of as grown $NdNiO_3/LaAlO_3$ (001) were characterized by scanning transmission electron microscopy (STEM) measurements in the high-angle annular dark-field (HAADF) mode. The resistivity of as-grown $NdNiO_3/LaAlO_3$ (001) was measured as a function of temperature using the Physical Property Measurement System (PPMS).

Nuclear reaction analysis

The nuclear reaction analysis (NRA) is the technique to quantitatively detect the hydrogen concentration based on the nuclear reaction between the $^{15}N^{2+}$ from accelerator and hydrogen (or proton). A nuclear reaction between the $^{15}N^{2+}$ incident ion beam and ^{1}H located at the material at a characteristic incident kinetic energy of ~6.385 MeV, and this release characteristic gamma-ray as to be detected to indicate the hydrogen concentration. To detect the ^{1}H depth profile, the kinetic energy of the incident $^{15}N^{2+}$ was increased from 6.385 MeV stepwise, in which case the nuclear reaction took place at a specific penetration depth according to a linear reduction in the kinetic energy of $^{15}N^{2+}$ with the penetration depth (~3.12 keV nm^{-1}). The depth resolution of NRA is of ~1 nm. [41]

In situ X-ray absorption spectroscopy measurements

The XANES data for Ni K-edge (8.31 keV-8.39 keV) were collected at room temperature in fluorescence mode using Hard X-ray Microfocus Beamline BL15U1 of the Shanghai Synchrotron Radiation Facility (SSRF). The synchrotron X-ray was first filtered by a nitrogen cooled double Si (111) crystal monochromator and then focused by a Kirkpatrick-Baez (KB) mirror with a beam size of $2.5 \times 2.5\ \mu m^2$ on the sample. During the measurement, the synchrotron was operated with a ring current of 200 mA, resulting in a photon flux of 1.1×10^{11} phs/s/μm^2 at the focal point. The incident photon energy was calibrated using a standard Ni metal foil prior to data collection. The fluorescent signals for each energy point were acquired by using Vortex®-90EX Silicon Drift Detector with an integration time of 3 seconds. The XANES spectra were obtained after energy calibration and normalization using the ATHENA packages.[49]

Conductive atomic force microscopy measurements

The conductive atomic force microscopy measurement (cAFM) was performed by a commercial scanning probe microscope (Cypher ES, Oxford Instruments) using conductive tips with a spring constant of about 2.8 N/m[45]. The ORCA mode and ORCA holder were used for current mapping. In the ORCA mode, the tips were virtually grounded, and the Pd electrode of the device is connected with the instrument through the Al wire as another end. A constant bias voltage of 0.5 V was applied to the sample during scanning. The ORCA holder used has a maximum current range of 10 μA and sensitivity of about 1 pA. The current in the area near the Pd electrode (approximately 0.1 μm) at 0.5 V bias is lower than the sensitivity of the instrument.

Applications of self-sensitizable neurons in fully connected spiking neural networks

We developed a self-sensitizable fully connected spiking neural network based on rate learning for image classification tasks using the Fashion MNIST datasets. This network utilizes the average firing rate of spiking neurons for learning. In this approach, the network encodes inputs as pulse events, propagates them through multiple simulated time steps, and derives the average firing rate of the neurons over the temporal sequence as the output. By assessing the loss between the output spiking rate and the label output, connection weights are adjusted using optimization algorithms such as gradient descent. This adjustment aims to bring the network's output closer to the expected values (input label). Rate learning-based spiking neural networks demonstrate robust learning performance with reduced computational complexity. More details about processing and training are provided in the **Supplemental experimental procedures.**

Fashion MNIST is a classic dataset used in the fields of machine learning and computer vision to evaluate and validate algorithms for image classification tasks. The Fashion MNIST dataset consists of images representing 10 different categories of fashion items, offering a more challenging task compared to the well-known MNIST dataset. Each category contains 7000 grayscale images of size 28x28 pixels. These categories include T-shirt, Trouser, Pullover, Dress, Coat, Sandal, Shirt, Sneaker, Bag, Ankle boot. The train set contains 60,000 labeled images, evenly distributed among the 10 categories. Each category has 6,000 training images. The test set contains 10,000 labeled images, also equally distributed across the 10 categories. Compared to the traditional MNIST dataset which consists of hand-written digits, Fashion MNIST is more challenging due to the greater diversity in appearance and structure of fashion items. This complexity poses a more intricate image classification task for algorithms.

Applications of self-sensitizable neurons in edge detection algorithm

We introduced a novel approach by applying the self-sensitizable neuron model to edge detection. The self-sensitizable neurons processes image gradient data obtained through the Sobel operator and dynamically adjusts their neural states based on distinct distributions of image gradient data. This characteristic enables the self-sensitizable neuron to maintain exceptional performance in edge detection of complex buildings and vehicles across diverse environments. The model incorporating self-sensitizable neurons underwent testing across different environments using a dataset generated by an AI painting model based on stable diffusion, primarily comprises four types of vehicles: sedans, sports utility vehicles (SUVs), pick-up trucks, and airplanes. Representative sample images can be found in the **Figure S13**. The dataset is divided into two distinct environments: bright and dark environments. Each environment consists of 1700 images, encompassing 500 images of sedans, 500 images of SUVs, 500 images of pick-up trucks, and 200 images of airplanes. Each of these images is a three-channel color image with 512×512 pixels. The distinction between vehicles and backgrounds varies in different environments, thereby allowing for an accurate assessment of the model algorithm's edge detection capabilities under varying conditions. To illustrate the differences more precisely in edge detection capabilities between different neurons, we utilized a Convolutional Neural Network (CNN) to classify the outputs of edge detection, providing a more intuitive representation of the distinction in the edge detection results. More details are available in **Supplemental experimental procedures**.

Applications of self-sensitizable neurons in spiking convolutional neural networks

The computational methodology employed in edge detection shares certain similarities with spiking convolutional neural networks (S-CNNs). Therefore, we integrated self-sensitizable neurons within the framework of S-CNNs. The S-CNN model was constructed using Pytorch. The convolutional layers were adapted from the conventional CNN model (Alex-Net) and transposed to the SNN framework. Through convolution and pooling operations, S-CNNs extract local features from images, imparting translation invariance and localized receptive fields to the network. The convolution and pooling operations facilitate parameter sharing, leading to a reduction in model parameters. This parameter sharing enhances the model's generalization capacity and efficiency.

We selected a subset of our custom dataset containing four distinct types of vehicles in bright environments for training. We simulated challenging dark scenarios by reducing image intensity and tested the network.

Then we employed Gradient-weighted Class Activation Mapping (Grad-CAM) to further investigate the decision-making process of the model. By combining the gradient information and feature maps of the model, we visualized the activation regions relevant to specific categories. Based on these results, we interpreted the advantages of the self-sensitizable S-CNN in adapting to changing environments from both a cognitive and decision-making perspective. Further elaboration can be found in **Supplemental experimental procedures**.

ACKNOWLEDGEMENTS

We acknowledge financial support from the National Key R&D Program of China (Nos. 2021YFA0718900 and 2022YFB3505600), the National Natural Science Foundation of China (Nos. 52271236, U22A20116, 52025024 and 12104005) and Beijing Natural Science Foundation (No. 4242058). The authors acknowledge Prof. Markus Wilde from the University of Tokyo for his useful discussion with the ion beam of nuclear reaction analysis. We also acknowledge Kejian Zhu and Xiaohua Sun at Beihang University for their contributions in sound recognition tasks in SNN. This work was carried out with the support of Shanghai Synchrotron Radiation Facility (SSRF) under proposal number 2023-SSRF-JJ-501887 and we gratefully acknowledge the beamline scientists (beamline BL15U1 at the SSRF) for their assistance with the in-situ micro-XAS experiments. M. Z. A. M. and A. S.'s work was supported in part by the National Science Foundation grant CCF no. 1955815. X. C. acknowledges the support from Scientific Research Foundation of the Higher Education Institutions for Distinguished Young Scholars in Anhui Province (Grants No. 2022AH020012), the Innovation Project for Overseas Researcher in Anhui Province (Grants No. 2022LCX004), and the start-up funding from Anhui University. Y. Yuan acknowledges the support from Shanghai Pujiang Program (22PJ1408400) and Shanghai Jiao Tong University 2030 Initiative.

AUTHOR CONTRIBUTIONS

H.-T. Z. conceived the study, designed the experiments, and supervised the project. H. Z. and J. C. grew the nickelate films and performed film related characterization. C. W. and X. C. fabricated the devices. T. Z. conducted all electrical measurements. M. H. performed the edge detection for buildings and vehicles based on fully-connected neural networks. M. H., M. Z. A. M. and A. S. performed object classification tasks with spiking convolutional neural networks. W. M., K. F., H. M. and J. C. performed the NRA measurements. Y. Y., T. Z., H. Z., K. Y., L. Z., J. W. and A. L. carried out the micro-XAS measurements. T. Z., L. W. and P. Y. performed the cAFM measurements. F. M. carried out the TEM characterization. W. Z. and S. L. helped with data analysis. H.-T. Z. and T. Z. wrote the manuscript. All authors participated in discussing and analyzing the results, as well as providing various reviews and comments for the paper.

DECLARATION OF INTERESTS

The authors declare no competing interests.

References

1. Wang, Z., Wu, H., Burr, G.W., Hwang, C.S., Wang, K.L., Xia, Q., and Yang, J.J. (2020). Resistive switching materials for information processing. Nat Rev Mater *5*, 173–195. 10.1038/s41578-019-0159-3.
2. Marković, D., Mizrahi, A., Querlioz, D., and Grollier, J. (2020). Physics for neuromorphic computing. Nat Rev Phys *2*, 499–510. 10.1038/s42254-020-0208-2.
3. Park, T.J., Deng, S., Manna, S., Islam, A.N.M.N., Yu, H., Yuan, Y., Fong, D.D., Chubykin, A.A., Sengupta, A., Sankaranarayanan, S.K.R.S., et al. (2022). Complex oxides for brain-inspired computing: A review. Adv Mater, 2203352. 10.1002/adma.202203352.
4. Smith, J.D., Hill, A.J., Reeder, L.E., Franke, B.C., Lehoucq, R.B., Parekh, O., Severa, W., and Aimone, J.B. (2022). Neuromorphic scaling advantages for energy-efficient random walk computations. Nat Electron *5*, 102–112. 10.1038/s41928-021-00705-7.
5. Sangwan, V.K., Liu, S.E., Trivedi, A.R., and Hersam, M.C. (2022). Two-dimensional materials for bio-realistic neuronal computing networks. Matter *5*, 4133–4152. 10.1016/j.matt.2022.10.017.
6. Pickett, M.D., Medeiros-Ribeiro, G., and Williams, R.S. (2013). A scalable neuristor built with Mott memristors. Nat Mater *12*, 114–117. 10.1038/nmat3510.
7. Kuzum, D., Jeyasingh, R.G.D., Lee, B., and Wong, H.S.P. (2012). Nanoelectronic programmable synapses based on phase change materials for brain-inspired computing. Nano Lett *12*, 2179–2186. 10.1021/nl201040y.
8. Milano, G., Pedretti, G., Montano, K., Ricci, S., Hashemkhani, S., Boarino, L., Ielmini, D., and Ricciardi, C. (2022). In materia reservoir computing with a fully memristive architecture based on self-organizing nanowire networks. Nat Mater *21*, 195–202. 10.1038/s41563-021-01099-9.

9. Kim, T.W., Choi, H., Oh, S.H., Jo, M., Wang, G., Cho, B., Kim, D.Y., Hwang, H., and Lee, T. (2009). Resistive switching characteristics of polymer non-volatile memory devices in a scalable via-hole structure. Nanotechnology *20*, 2. 10.1088/0957-4484/20/2/025201.
10. Wang, W., Danial, L., Li, Y., Herbelin, E., Pikhay, E., Roizin, Y., Hoffer, B., Wang, Z., and Kvatinsky, S. (2022). A memristive deep belief neural network based on silicon synapses. Nat Electron *5*, 870–880. 10.1038/s41928-022-00878-9.
11. Zhang, X., Wu, S., Yu, R., Li, E., Liu, D., Gao, C., Hu, Y., Guo, T., and Chen, H. (2022). Programmable neuronal-synaptic transistors based on 2D MXene for a high-efficiency neuromorphic hardware network. Matter *5*, 3023–3040. 10.1016/j.matt.2022.06.009.
12. Liu, X., Katti, K., and Jariwala, D. (2023). Accelerate & Actualize: Can 2D materials bridge the gap between neuromorphic hardware and the human brain? Matter *6*, 1348–1365. 10.1016/j.matt.2023.03.016.
13. Yi, S. in, Kendall, J.D., Williams, R.S., and Kumar, S. (2023). Activity-difference training of deep neural networks using memristor crossbars. Nat Electron *6*, 45–51. 10.1038/s41928-022-00869-w.
14. Abraham John, R., Milozzi, A., Tsarev, S., Brönnimann, R., Boehme, S.C., Wu, E., Shorubalko, I., Kovalenko, M. V, and Ielmini, D. (2022). Ionic-electronic halide perovskite memdiodes enabling neuromorphic computing with a second-order complexity. Sci Adv *8*, eade0072. 10.1126/sciadv.ade0072.
15. Ohno, T., Hasegawa, T., Tsuruoka, T., Terabe, K., Gimzewski, J.K., and Aono, M. (2011). Short-term plasticity and long-term potentiation mimicked in single inorganic synapses. Nat Mater *10*, 591–595. 10.1038/nmat3054.
16. Kudithipudi, D., Aguilar-Simon, M., Babb, J., Bazhenov, M., Blackiston, D., Bongard, J., Brna, A.P., Chakravarthi Raja, S., Cheney, N., Clune, J., et al. (2022). Biological underpinnings for lifelong learning machines. Nat Mach Intell *4*, 196–210. 10.1038/s42256-022-00452-0.
17. Yi, W., Tsang, K.K., Lam, S.K., Bai, X., Crowell, J.A., and Flores, E.A. (2018). Biological plausibility and stochasticity in scalable VO_2 active memristor neurons. Nat Commun *9*, 1. 10.1038/s41467-018-07052-w.
18. Deco, G., Rolls, E.T., and Romo, R. (2009). Stochastic dynamics as a principle of brain function. Prog Neurobiol *88*, 1–16. 10.1016/j.pneurobio.2009.01.006.
19. Markram, H. (2006). The blue brain project. Nat Rev Neurosci *7*, 153–160. 10.1038/nrn1848.
20. Wang, Z., Joshi, S., Savel'ev, S.E., Jiang, H., Midya, R., Lin, P., Hu, M., Ge, N., Strachan, J.P., Li, Z., et al. (2017). Memristors with diffusive dynamics as synaptic emulators for neuromorphic computing. Nat Mater *16*, 101–108. 10.1038/nmat4756.
21. Tuma, T., Pantazi, A., Le Gallo, M., Sebastian, A., and Eleftheriou, E. (2016). Stochastic phase-change neurons. Nat Nanotechnol *11*, 693–699. 10.1038/nnano.2016.70.
22. Chen, H., Xue, X., Liu, C., Fang, J., Wang, Z., Wang, J., Zhang, D.W., Hu, W., and Zhou, P. (2021). Logic gates based on neuristors made from two-dimensional materials. Nat Electron *4*, 399–404. 10.1038/s41928-021-00591-z.

23. Rao, A., Plank, P., Wild, A., and Maass, W. (2022). A long short-term memory for AI applications in spike-based neuromorphic hardware. Nat Mach Intell *4*, 467–479. 10.1038/s42256-022-00480-w.
24. Kwon, D., Woo, S.Y., Lee, K.-H., Hwang, J., Kim, H., Park, S.-H., Shin, W., Bae, J.-H., Kim, J.-J., and Lee, J.-H. (2023). Reconfigurable neuromorphic computing block through integration of flash synapse arrays and super-steep neurons. Sci Adv *9*, eadg9123. 10.1126/sciadv.adg9123.
25. Govardovskii, V.I., Calvert, P.D., and Arshavsky, V.Y. (2000). Commentary photoreceptor light adaptation: Untangling desensitization and sensitization. J. Gen. Physiol *116*, 791–794. 10.1085/jgp.116.6.791.
26. Khalighinejad, B., Herrero, J.L., Mehta, A.D., and Mesgarani, N. (2019). Adaptation of the human auditory cortex to changing background noise. Nat Commun *10*, 2509. 10.1038/s41467-019-10611-4.
27. Willmore, B.D.B., and King, A.J. (2023). Adaptation in auditory processing. Physiol Rev *103*, 1025–1058. 10.1152/physrev.00011.2022.
28. Azouz, R., Gray, C.M., and Glaser, D.A. (2000). Dynamic spike threshold reveals a mechanism for synaptic coincidence detection in cortical neurons in vivo. Proc. Natl. Acad. Sci. U.S.A *97*, 8110–8115. 10.1073/pnas.130200797.
29. D.A Henze, G.B. (2001). Action potential threshold of hippocampal pyramidal cells in vivo is increased by recent spiking activity. Neuroscience *105*. 10.1016/S0306-4522(01)00167-1.
30. Shaban, A., Bezugam, S.S., and Suri, M. (2021). An adaptive threshold neuron for recurrent spiking neural networks with nanodevice hardware implementation. Nat Commun *12*, 4234. 10.1038/s41467-021-24427-8.
31. Xu, Y., Gao, S., Li, Z., Yang, R., and Miao, X. (2022). Adaptive Hodgkin–Huxley neuron for retina-inspired perception. Adv Intell Syst *4*, 2200210. 10.1002/aisy.202200210.
32. S. Bianchi, I. Muńoz-Martín, S. Hashemkhani, G. Pedretti and D. Ielmini. (2020). A bio-inspired recurrent neural network with self-adaptive neurons and PCM synapses for solving reinforcement learning tasks. 2020 IEEE International Symposium on Circuits and Systems *(ISCAS)* 1-5. 10.1109/ISCAS45731.2020.9181103.
33. X. Wang, P. Huang, Z. Dong, Z. Zhou, Y. Jiang, R. Han, L. Liu, X. Liu, J. Kang. (2018). A novel RRAM-based adaptive-threshold LIF neuron circuit for high recognition accuracy. 2018 International Symposium on VLSI Technology, Systems and Application *(VLSI-TSA)* 1-2. 10.1109/VLSI-TSA.2018.8403854.
34. Deng, S., Park, T.J., Yu, H., Saha, A., Nafiul Islam, A.N.M., Wang, Q., Sengupta, A., and Ramanathan, S. (2023). Hydrogenated VO_2 bits for probabilistic computing. IEEE Electron Device Letters, 1–1. 10.1109/LED.2023.3303875.
35. Jiang, Y., Wang, D., Lin, N., Shi, S., Zhang, Y., Wang, S., Chen, X., Chen, H., Lin, Y., Loong, K.C., et al. (2023). Spontaneous threshold lowering neuron using second-order diffusive memristor for self-adaptive spatial attention. Adv Sci, 10, 2301323. 10.1002/advs.202301323.
36. Catalan, G. (2008). Progress in perovskite nickelate research. Phase Transit *81*, 729–749. 10.1080/01411590801992463.

37. Ramadoss, K., Zuo, F., Sun, Y., Zhang, Z., Lin, J., Bhaskar, U., Shin, S., Alam, M.A., Guha, S., Weinstein, D., et al. (2018). Proton-doped strongly correlated perovskite nickelate memory devices. IEEE Electron Device Letters *39*, 1500–1503. 10.1109/LED.2018.2865776.
38. Shi, J., Zhou, Y., and Ramanathan, S. (2014). Colossal resistance switching and band gap modulation in a perovskite nickelate by electron doping. Nat Commun *5*, 4860. 10.1038/ncomms5860.
39. Oh, C., Heo, S., Jang, H.M., and Son, J. (2016). Correlated memory resistor in epitaxial $NdNiO_3$ heterostructures with asymmetrical proton concentration. Appl Phys Lett 108. 122106. 10.1063/1.4944842.
40. Zhang, H.T., Park, T.J., Zaluzhnyy, I.A., Wang, Q., Wadekar, S.N., Manna, S., Andrawis, R., Sprau, P.O., Sun, Y., Zhang, Z., et al. (2020). Perovskite neural trees. Nat Commun *11*, 2245. 10.1038/s41467-020-16105-y.
41. Chen, J., Mao, W., Ge, B., Wang, J., Ke, X., Wang, V., Wang, Y., Döbeli, M., Geng, W., Matsuzaki, H., et al. (2019). Revealing the role of lattice distortions in the hydrogen-induced metal-insulator transition of $SmNiO_3$. Nat Commun *10*, 694. 10.1038/s41467-019-08613-3.
42. Wilde, M., and Fukutani, K. (2014). Hydrogen detection near surfaces and shallow interfaces with resonant nuclear reaction analysis. Surf Sci Rep *69*, 196–295. 10.1016/j.surfrep.2014.08.002.
43. Lanford, W.A., Trautvetter, H.P., Ziegler, J.F., and Keller, J. (1976). New precision technique for measuring the concentration versus depth of hydrogen in solids. Appl Phys Lett *28*, 566–568. 10.1063/1.88826.
44. Zhou, Y., Guan, X., Zhou, H., Ramadoss, K., Adam, S., Liu, H., Lee, S., Shi, J., Tsuchiya, M., Fong, D.D., et al. (2016). Strongly correlated perovskite fuel cells. Nature *534*, 231–234. 10.1038/nature17653.
45. Li, L., Wang, M., Zhou, Y., Zhang, Y., Zhang, F., Wu, Y., Wang, Y., Lyu, Y., Lu, N., Wang, G., et al. (2022). Manipulating the insulator–metal transition through tip-induced hydrogenation. Nat Mater *21*, 1246–1251. 10.1038/s41563-022-01373-4.
46. Duan, Q., Jing, Z., Zou, X., Wang, Y., Yang, K., Zhang, T., Wu, S., Huang, R., and Yang, Y. (2020). Spiking neurons with spatiotemporal dynamics and gain modulation for monolithically integrated memristive neural networks. Nat Commun *11*, 3399. 10.1038/s41467-020-17215-3.
47. Zhang, H.T., Park, T.J., Islam, A.N.M.N., Tran, D.S.J., Manna, S., Wang, Q., Mondal, S., Yu, H., Banik, S., Cheng, S., et al. (2022). Reconfigurable perovskite nickelate electronics for artificial intelligence. Science 375. 533-539. 10.1126/science.abj7943.
48. Li, H., Wang, Y., Meng, F., Mao, W., Cao, X., Bian, Y., Zhang, H., Jiang, Y., Chen, N., and Chen, J. (2023). Metal-organic decomposition growth of thin film metastable perovskite nickelates with kinetically improved quantum transitions. Int J Miner Metall Mater. 10.1007/s12613-023-2703-9.
49. Ravel, B., and Newville, M. (2005). ATHENA, ARTEMIS, HEPHAESTUS: Data analysis for X-ray absorption spectroscopy using IFEFFIT. J Synchrotron Radiat, pp. 537–541. 10.1107/S0909049505012719.

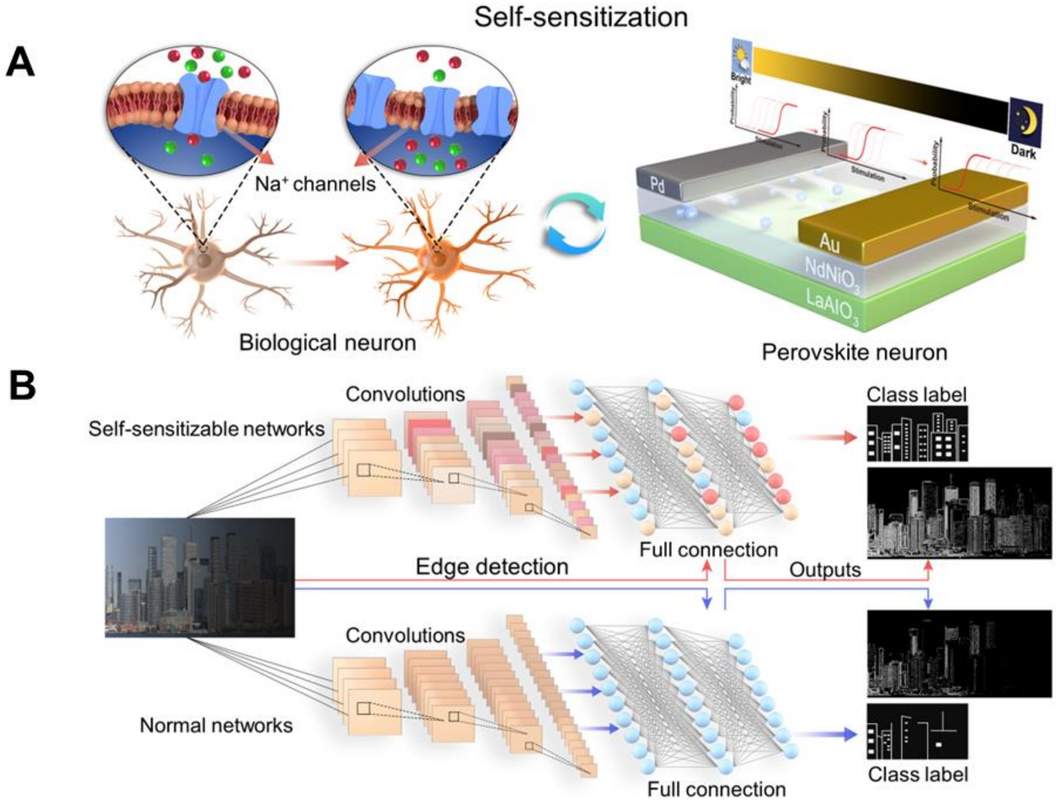

Figure 1. Self-sensitization and applications in AI. (A) Schematic of the biological neuron sensitization and the hydrogen-doped perovskite nickelate device. In biological nervous system, increased availability of sodium channels facilitates the subsequent generation of potential difference across the neuron's membrane, thereby reducing the neuron threshold and enabling the neuron to sensitively respond to weaker signals. The functionality of the self-sensitizable neuron can be implemented on a single hydrogen-doped $NdNiO_3$ device, where the proton gradient can precisely react to electric pulses, leading to different neuron activation functions and signal reception abilities. **(B)** Applications of self-sensitizable perovskite neurons in edge detection and classification tasks. The networks with self-sensitizable neurons exhibit improved performance through adaptively adjusting activation functions to capture more detailed edge information and distinct object features in ever-changing environments.

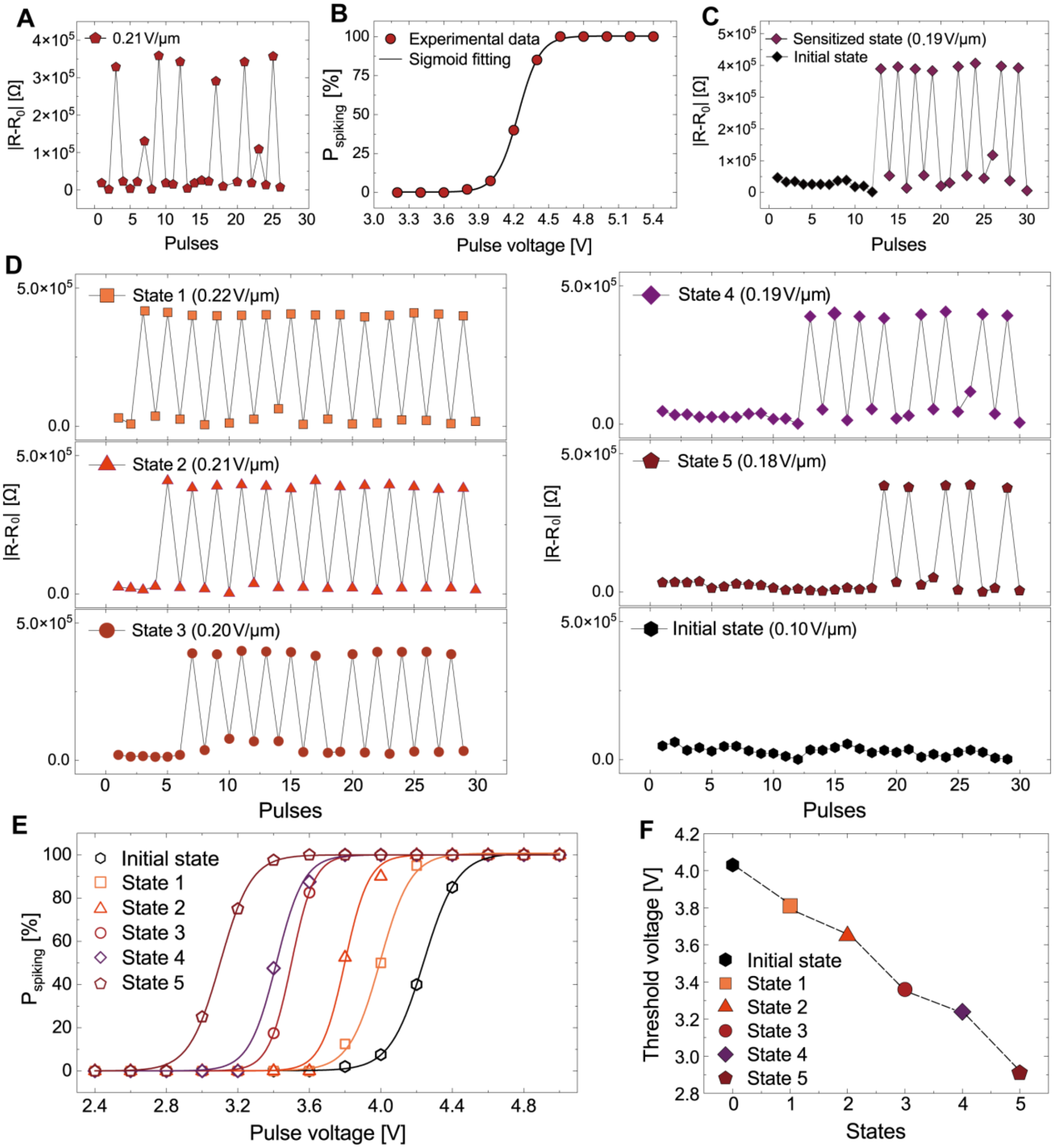

Figure 2. Electrical characterization of the self-sensitizable stochastic perovskite neuron. (A) The perovskite nickelate neurons exhibited stochastic spiking behaviors under electric pulses (0.21 V/μm for 100 μs). The stochastic neuron can generate spikes with a sudden resistance change under electric field pulses. The occurrence of these spikes is stochastic and dependent on the magnitude of the electric field. The combination of an electric pulse and a reverse pulse was employed to ensure that the results of each pulse action do not interfere with each other. **(B)** Spiking probability of the perovskite neuron as a function of pulse voltages. The solid line represents a sigmoid fitting that is commonly observed in the biological neural system. The spiking

probabilities were obtained by sampling over 30 pulsing events for each pulse voltage. **(C)** With the accumulation of weak pulses (0.19 V/μm for 100 μs) without any reset pulse, the neuron spiking probability increased significantly in response to the same electric pulse magnitude, which means the neuron can adaptively capture the previously unrecognized signal. The black part represents the initial state before the self-sensitization and the purple part represents the self-sensitized state. **(D)** By accumulating different electric pulse fields with the same pulse width, the artificial neuron achieved different self-sensitized states to capture a broader range of weak signals. Furthermore, it can filter out weaker signals selectively, preventing the device from being disrupted by background noise. **(E)** Spiking probabilities of different sensitized states as shown in **(D),** which suggests that the neuron can adaptively exhibit varying degrees of adjustment based on different input signals. **(F)** The threshold voltages for different sensitized states extrapolated from **(E),** where the neuron exhibits different degrees of neuron activation function shift in response to diverse external signals. The pulse voltage at which the perovskite neuron exhibits a spiking probability of 10% is defined as its spiking threshold.

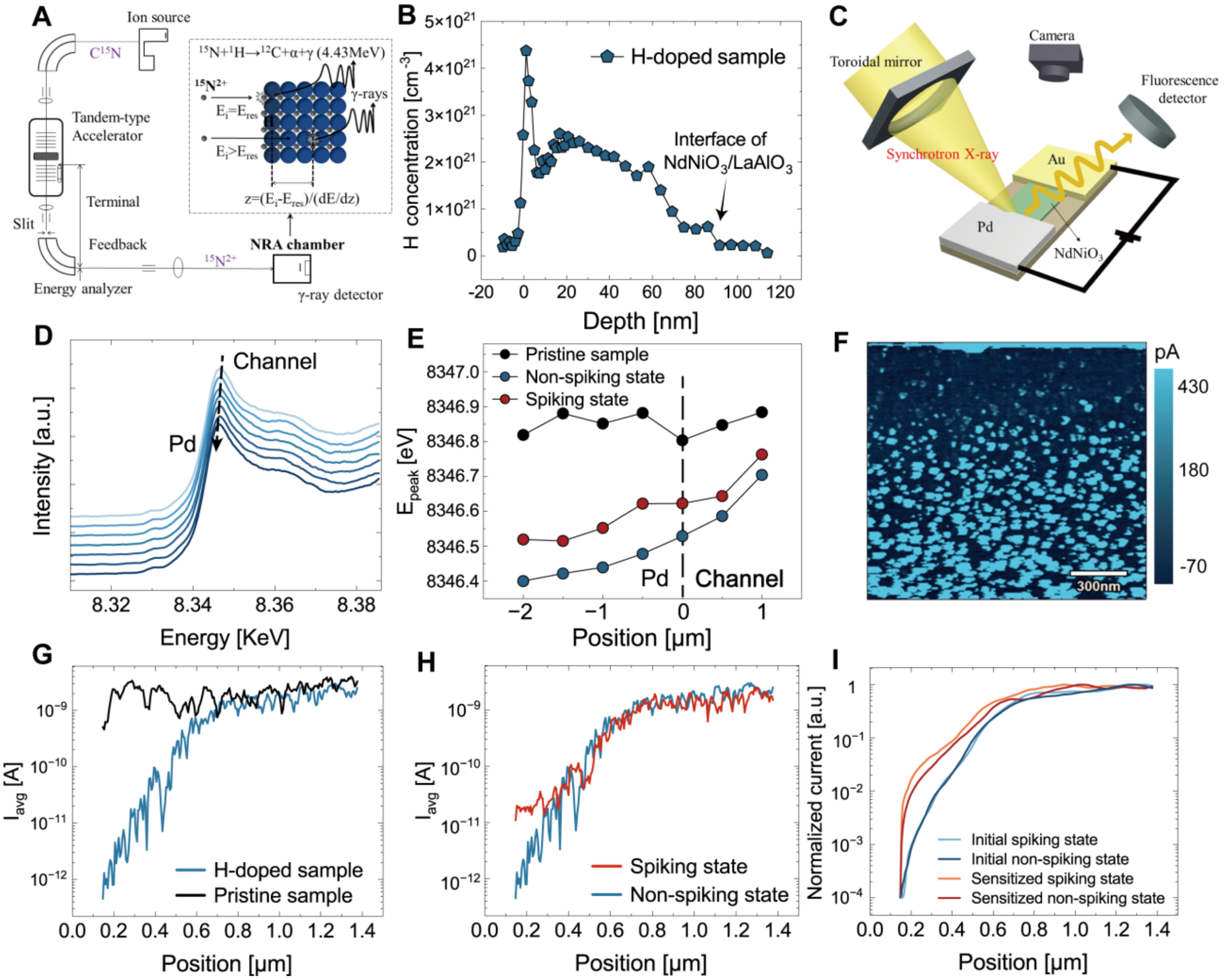

Figure 3. Microscopic mechanism of the self-sensitization in a perovskite neuron. (A) Schematic of the nuclear reaction analysis (NRA) which can quantify the absolute amount of hydrogen within a solid. **(B)** The hydrogen content exhibited a gradient distribution from the surface to the film-substrate interface. It is worth noting that the distinct minima and maxima of hydrogen concentration near the film surface are attributed to the influence of the instrumental function of the NRA and native hydrogen absorbed by the surface. **(C)** Schematic of the micro-X-ray absorption spectroscopy measurement. The incoming X-ray beam is focused on different positions near the Pd electrode. The fluorescence signal is recorded by a detector positioned perpendicular to the X-ray beam. **(D)** The X-ray absorption spectra were measured at different positions on the device, ranging from the device channel (top) to the Pd electrode (bottom). The curves illustrate the variation of the Ni K-edge XAS spectra, and the dashed line is used as a guide to visualize the peak shift. The shift of the peak towards lower energies indicates a change in the valence state of Ni, which can be attributed to the variation in hydrogen gradient. **(E)** The Ni K-edge peak positions for the pristine sample (no H-doping) and different neuron states along the device channel. No peak shift was observed in the pristine sample, while a noticeable difference in peak shift was found between the non-spiking state and the spiking state, indicating distinct

changes in Ni valence and the distribution of hydrogen gradient. The dashed line represents the edge of the Pd electrode. **(F)** Current maps obtained in the conducting atomic force microscopy (cAFM) experiments by scanning near the Pd electrode (top of the figure), and the current gradient near the Pd electrode was observed for a H-doped sample. The tested area has a size of 1.5 μm^2 with 256×256 pixels. **(G)** Mean current values were plotted as a function of position along the channel direction. Gradual decrease in current observed in the H-doped sample indicates the presence of a hydrogen gradient within the NNO channel. **(H)** Mean current values for the non-spiking state and the spiking state of the perovskite neuron, with a difference in current by one order of magnitude near the Pd electrode. **(I)** Difference in normalized current distribution between the initial state and the sensitized state indicates that the sensitizing field (0.19 V/μm) altered the distribution of hydrogen gradient.

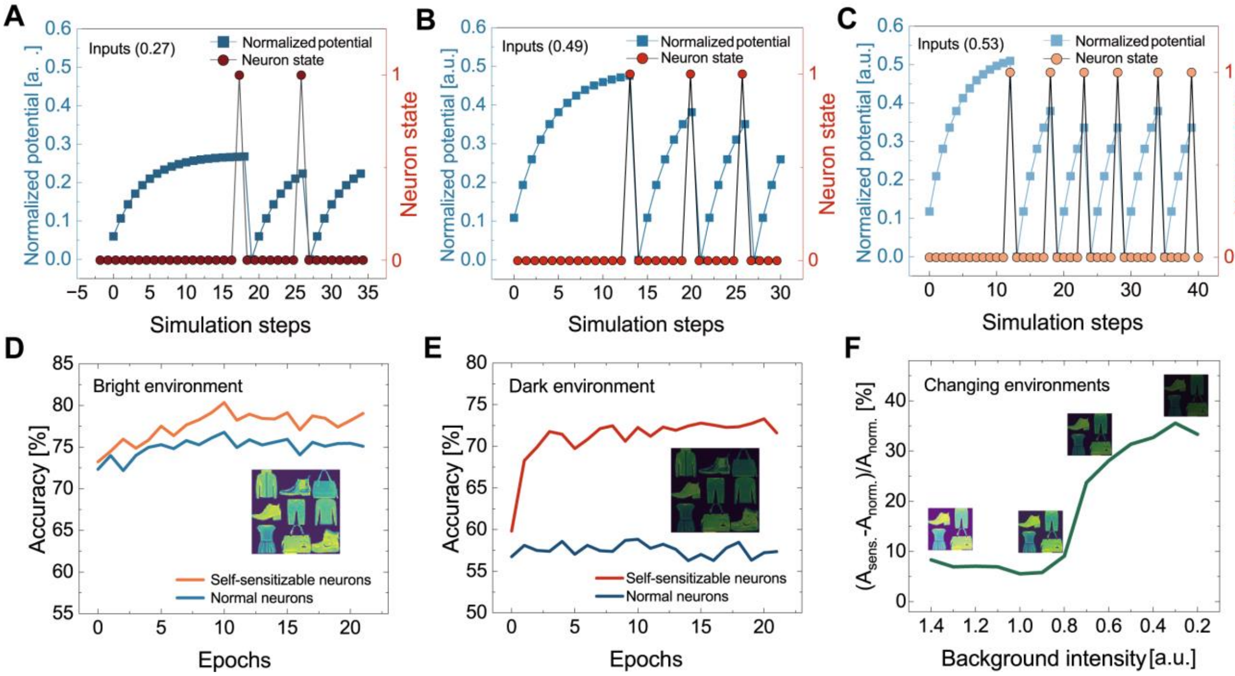

Figure 4. Practicality test of the self-sensitizable neurons. (A)-(C) Simulation based on experimentally measured neuron activation function shifts of perovskite neurons. The neuron model exhibits varying degrees of self-sensitization to different normalized inputs. **(D)** The classification accuracy of the self-sensitizable and normal networks (both without convolutional layers) on the standard Fashion MNIST dataset in bright environment. **(E)** Significant accuracy improvement of the self-sensitizable networks compared to normal networks in dark environment. **(F)** The advantages of the self-sensitizable networks becomes increasingly evident as the brightness of the environment continuously changes.

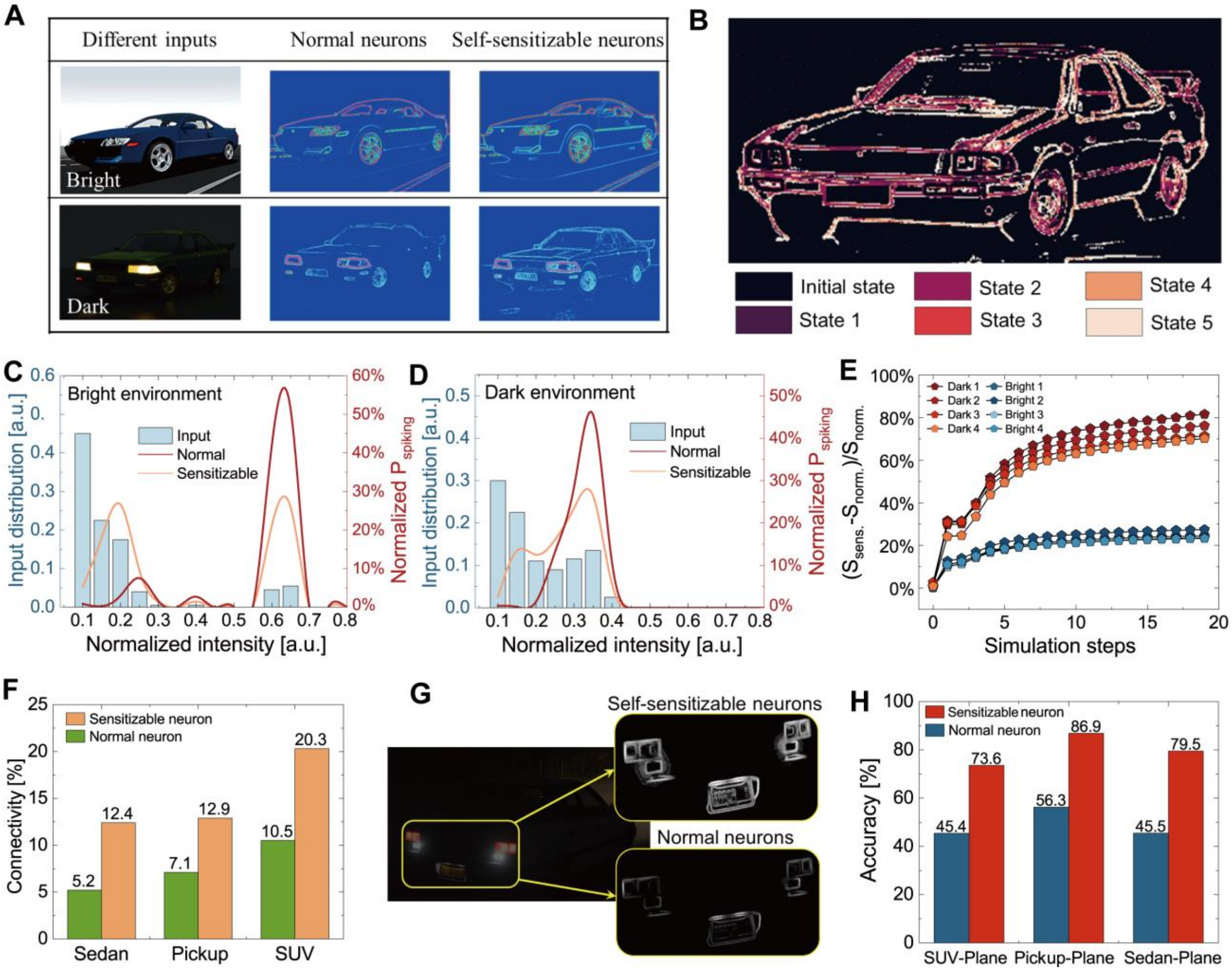

Figure 5. Applications of self-sensitizable neurons in vehicle edge detections. **(A)** Vehicle edge detection using self-sensitizable or normal neurons in both bright and dark environments. The networks with self-sensitizable neurons exhibited good performance in different environments, surpassing the networks with normal neurons. **(B)** Complete edge information captured by different adaptive states of self-sensitizable neurons. These neuron states in the networks are from the experimental measurements of the self-sensitizable perovskite neuron. **(C)** and **(D)** The distributions of signal intensity in different environments and the corresponding spiking probability of normal neurons and self-sensitizable neurons. The spiking probability in **c** suggests that the self-sensitizable networks redistributed the computing resources in bright environments to enhance the sensitivity to detailed information. **(D)** illustrates that the self-sensitizable networks reshaped the signal reception range in dark environments with an additional spiking probability peak, capturing the weak information that normal networks failed to recognize. **(E)** Increased spiking numbers of self-sensitizable neurons compared to normal neurons across different images in bright and dark environments (Bright1, Dark1, Bright2, Dark2, etc.) showcases the adaptability of self-sensitizable neurons in efficiently processing weak signals under diverse environmental conditions. **(F)** The edge connectivity of different vehicles when transitioning into dark environments, calculated by averaging the connectivity from 100 results of different vehicle detections. **(G)** The self-sensitizable network can adaptively capture detailed information of

license plate numbers when shifting into dark surroundings, exhibiting the potential to operate effectively in complex real-world environments. **(H)** Significant increase in accuracy of self-sensitizable neurons in classifying SUVs, pickup trucks, sedans, and airplanes, compared to the normal neurons.

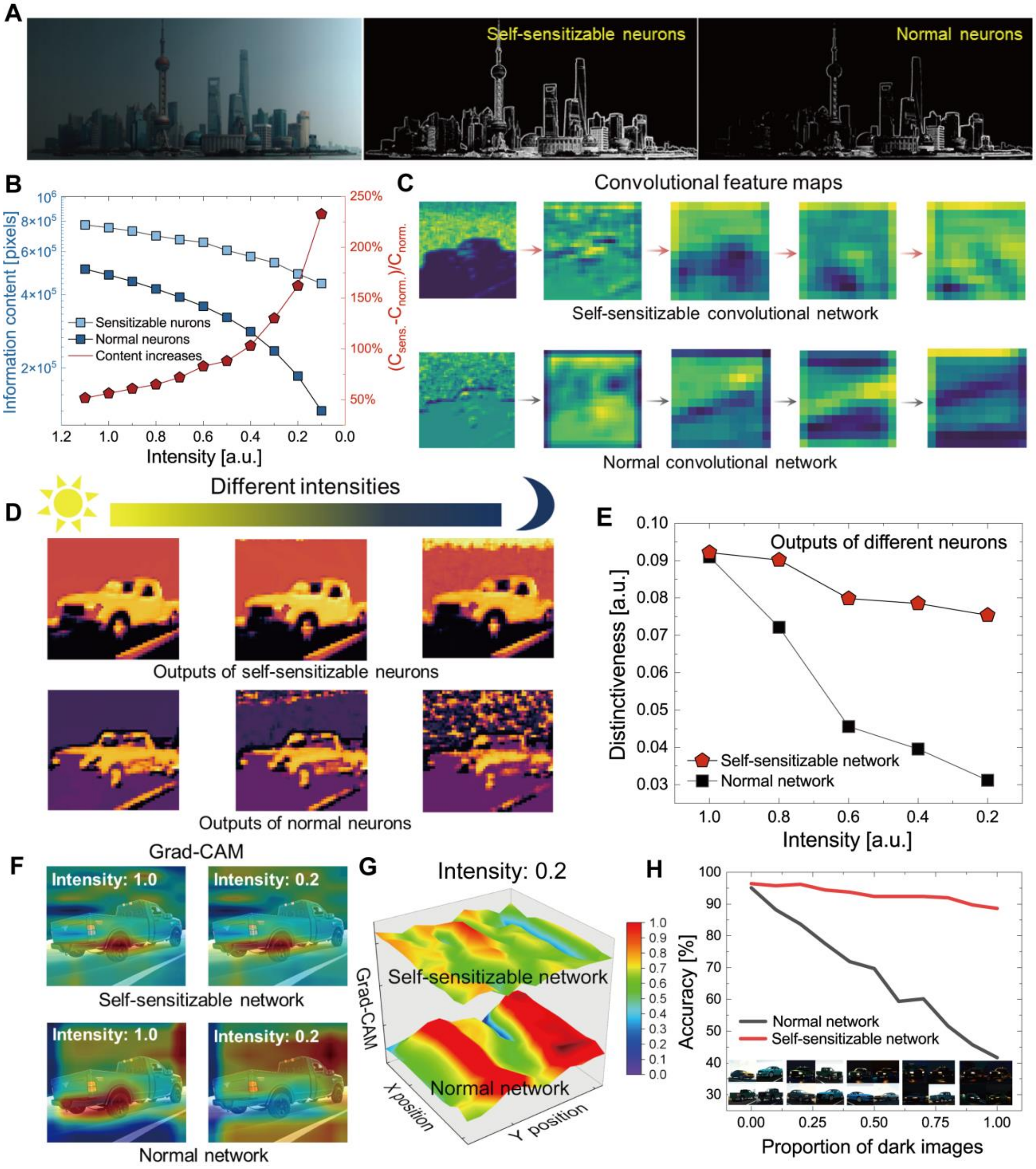

Figure 6. Applications of self-sensitizable convolutional neural networks in classification tasks. (A) Self-sensitizable neurons empower the networks to capture more information in ever-changing environments, allowing for complete object recognition. **(B)** The networks with self-sensitizable neurons can extract more information content in dynamic environments, exceeding normal networks by ~250% when transitioning into dark surroundings. **(C)** The convolutional feature maps of the self-sensitizable networks and the normal networks when classifying images after transitioning to low-light environments. The self-sensitizable convolutional layers can extract

more distinct features. **(D)** The outputs of the convolutional neurons in two types of networks. The self-sensitizable neurons can adaptively reshape the information reception range to maintain the subject-environment distinctiveness in ever-changing surroundings. In contrast, the normal neurons struggled to discern the environment and the subject clearly when transitioning into dark environments. **(E)** Comparing the outputs of different neurons to assess subject-environment distinctiveness. The self-sensitizable network maintained a robust ability to distinguish subject and environment across varying environmental intensities. **(F)** and **(G)** Gradient-weighted Class Activation Mapping (Grad-CAM) associates classification decisions with different regions of the input images, enabling a clear visualization of the primary contributing regions to the classification result. The red portions in the images represent crucial features guiding the classification. **(H)** Vehicle image classification tasks with different proportions of bright and dark environments. The self-sensitizable convolutional network maintained a high classification accuracy, while the accuracy of the normal network diminished significantly.